

# Imaging individual neurons in the retinal ganglion cell layer of the living eye

Ethan A. Rossi<sup>a,1,2</sup>, Charles E. Granger<sup>a,b,3</sup>, Robin Sharma<sup>a,3</sup>, Qiang Yang<sup>a</sup>, Kenichi Saito<sup>c</sup>, Christina Schwarz<sup>a</sup>, Sarah Walters<sup>a,b</sup>, Koji Nozato<sup>c</sup>, Jie Zhang<sup>a</sup>, Tomoaki Kawakami<sup>c</sup>, William Fischer<sup>d</sup>, Lisa R. Latchney<sup>d</sup>, Jennifer J. Hunter<sup>a,d</sup>, Mina M. Chung<sup>a,d</sup>, and David R. Williams<sup>a,b</sup>

<sup>a</sup>Center for Visual Science, University of Rochester, Rochester, NY 14642; <sup>b</sup>The Institute of Optics, University of Rochester, Rochester, NY 14620; <sup>c</sup>Canon USA, Inc., Melville, NY 11747; and <sup>d</sup>Flaum Eye Institute, University of Rochester Medical Center, Rochester, NY 14642

Edited by Stephen Burns, Indiana University System, Bloomington, IN, and accepted by Editorial Board Member Jeremy Nathans December 6, 2016 (received for review August 19, 2016)

Although imaging of the living retina with adaptive optics scanning light ophthalmoscopy (AOSLO) provides microscopic access to individual cells, such as photoreceptors, retinal pigment epithelial cells, and blood cells in the retinal vasculature, other important cell classes, such as retinal ganglion cells, have proven much more challenging to image. The near transparency of inner retinal cells is advantageous for vision, as light must pass through them to reach the photoreceptors, but it has prevented them from being directly imaged *in vivo*. Here we show that the individual somas of neurons within the retinal ganglion cell (RGC) layer can be imaged with a modification of confocal AOSLO, in both monkeys and humans. Human images of RGC layer neurons did not match the quality of monkey images for several reasons, including safety concerns that limited the light levels permissible for human imaging. We also show that the same technique applied to the photoreceptor layer can resolve ambiguity about cone survival in age-related macular degeneration. The capability to noninvasively image RGC layer neurons in the living eye may one day allow for a better understanding of diseases, such as glaucoma, and accelerate the development of therapeutic strategies that aim to protect these cells. This method may also prove useful for imaging other structures, such as neurons in the brain.

imaging | adaptive optics | retinal ganglion cells | photoreceptors | retina

Light traverses several layers of nearly transparent neurons before reaching the photopigment in the photoreceptors, initiating the first step in seeing. Information from photoreceptors is then relayed back through this tissue and processed by numerous parallel neural circuits before reaching the retinal ganglion cells (RGCs), whose axons form the optic nerve (1). Retinal disease can impact any of several classes of retinal neurons. However, vision loss from the diseases that cause the most cases of acquired blindness in the world (2), age-related macular degeneration (AMD) and glaucoma, is primarily due to the progressive death of photoreceptors (3, 4) and RGCs (5), respectively. Although adaptive optics (AO) ophthalmoscopy can image photoreceptors, their survival can be uncertain when pathology has altered the retina. RGCs and other inner retinal neurons have proven difficult to image directly, even with AO (6). New methods are needed to monitor these cell classes on a microscopic scale in the living eye to better understand the pathogenesis and progression of these diseases and detect them earlier, before irreversible cell death occurs.

Ordinary fundus cameras lack the axial resolution to selectively image the different layers of the retina. Optical coherence tomography, the standard for clinical assessment of RGCs in glaucoma (7), permits gross measurement of all RGC axons together [i.e., retinal nerve fiber layer (RNFL) thickness]. However, segmenting just the RGC layer is difficult (8) and conventional optical coherence tomography lacks the transverse resolution to evaluate individual cells. A statistically significant RNFL thinning, indicative of glaucomatous damage, may represent the death of tens of thousands or even hundreds of thousands of RGCs (9). A

noninvasive *in vivo* imaging method permitting early detection of morphological changes in RGCs at a cellular or subcellular level would be transformative for understanding the early pathogenetic mechanisms of glaucoma and facilitate earlier diagnosis and treatment (6).

AO enables near diffraction-limited imaging in the living eye (10, 11). AO scanning light ophthalmoscopy (AOSLO) (12) has been used to investigate how our visual capabilities are formed from discrete sampling by individual cones (13, 14), and how disease alters the living retina at a cellular level (15–18). AOSLO has proven to be a powerful platform for translating existing microscopy and ophthalmoscopy methods for high-resolution *in vivo* imaging. Off-axis detection methods, such as “dark-field” (19), “offset-aperture” (20), and “split-detection” (21) have been adapted to AOSLO to image the retinal pigment epithelium (22), blood vessel walls (23), and putative cone inner segments (24). Split-detection resolved uncertainty about cone survival in achromatopsia (24) and may be useful for doing the same in AMD. However, despite these continuous advances, several types of retinal cells, including Müller, bipolar, horizontal, amacrine, and RGCs have remained inaccessible to imaging in humans.

Intrinsic two-photon excitation fluorescence (25) (TPEF) was recently deployed in AOSLO to image monkeys and resolved structural features at multiple retinal layers. Contrast is achieved

## Significance

Retinal ganglion cells are the primary output neurons of the retina that process visual information and transmit it to the brain. We developed a method to reveal these cells in the living eye that does not require the fluorescent labels or high light levels that characterize more invasive methods. The death of these cells causes vision loss in glaucoma, the second leading cause of blindness worldwide. The ability to image these cells in the living eye could accelerate our understanding of their role in normal vision and provide a diagnostic tool for evaluating new therapies for retinal disease.

Author contributions: E.A.R. designed research; E.A.R., C.E.G., R.S., K.S., C.S., S.W., K.N., J.Z., T.K., W.F., L.R.L., and M.M.C. performed research; E.A.R. and Q.Y. contributed new reagents/analytic tools; E.A.R., C.E.G., R.S., K.S., and K.N. analyzed data; E.A.R., C.E.G., R.S., K.S., C.S., S.W., J.J.H., M.M.C., and D.R.W. wrote the paper; and D.R.W. supervised the project.

Conflict of interest statement: E.A.R. has filed patent applications on aspects of the technology described in this manuscript. D.R.W. and Q.Y. have patents on aspects of the technology described in this manuscript. Some of D.R.W.’s patents have been licensed by Canon, Inc.

This article is a PNAS Direct Submission. S.B. is a Guest Editor invited by the Editorial Board.

Freely available online through the PNAS open access option.

<sup>1</sup>Present address: Department of Ophthalmology, School of Medicine, University of Pittsburgh, Pittsburgh, PA 15213.

<sup>2</sup>To whom correspondence should be addressed. Email: rossiea@pitt.edu.

<sup>3</sup>C.E.G. and R.S. contributed equally to this work.

This article contains supporting information online at [www.pnas.org/lookup/suppl/doi:10.1073/pnas.1613445114/-DCSupplemental](http://www.pnas.org/lookup/suppl/doi:10.1073/pnas.1613445114/-DCSupplemental).

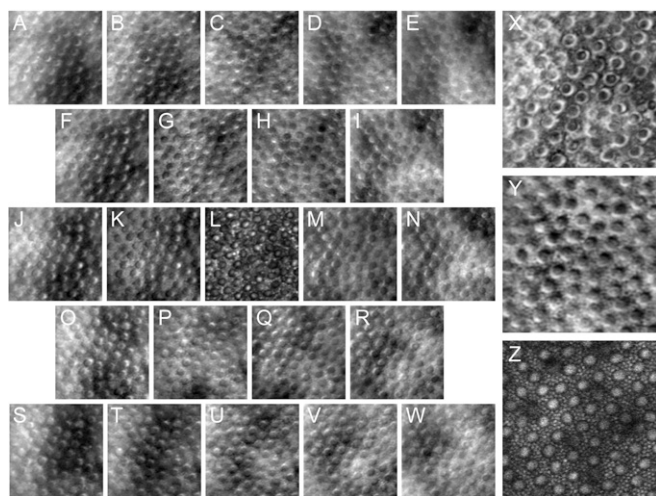


**Fig. 1.** Offset-aperture images (A–K and M–W) show characteristic intensity gradients across cones. Images positioned to reflect sampling pattern (aperture:  $\sim 4$  ADD; offset:  $\sim 8$ –21 ADD). SD of offset-aperture images (X) reflects asymmetry as cones appear as rings. Differencing enhances contrast; Y is the difference of P and H. Confocal (L) and TPEF (Z) shown for comparison. Light was focused to maximum cone TPEF, assumed to be at plane of cone outer segments. Images are  $100 \times 100 \mu\text{m}$ .

by heterogeneous distribution of endogenous fluorophores. TPEF revealed Müller cells and RGC layer neurons in monkeys and was validated through *ex vivo* tissue comparisons (26). However, a significant limitation of TPEF is the need for high light levels that restrict its use to animals. More work is needed to optimize TPEF for safe human imaging. In the meantime, off-axis detection methods offer promise for imaging these cells.

These methods share the property that they integrate photons from regions of the retinal conjugate focal plane other than that sampled by the usual confocal pinhole centered on the optical axis, and differ primarily in the specific regions light is detected from and in the number of detectors used (Fig. S1). The explanation for the difference between these modalities and conventional on-axis confocal imaging put forth by Elsner et al., is that shifting detection away from the optical axis increases the fraction of light reaching the detector that is multiply scattered by the retina (20, 23, 27). Here we sought through empirical investigations to better understand how detection can be optimized to image the nearly transparent inner retina.

We used the simplest off-axis detection scheme, offset-aperture (20, 23), and explored how offset distance (that we extend to positions far beyond those previously measured), offset direction, and aperture size impacted image content in both monkeys and humans. We then combined images from different aperture positions to enhance structural contrast. Because our ultimate goal was to image RGCs in humans but we had no secondary mechanism to identify these cells (e.g., TPEF), we imaged macaque monkeys, an animal with a retina similar to humans, using simultaneous TPEF (26) to validate the approach. Here we show that by combining multiple offset-aperture images, structural contrast can be enhanced through the entire retinal thickness and that the somas of individual cells within the RGC layer can be revealed using this “multioffset” approach.

## Results

**Outer Retina.** Individual rods and cones were visible at all offsets (Fig. 1 A–K and M–W) in monkeys, albeit with variable contrast as signal intensity dropped considerably with increasing offset. Cones were clearly discernable and in register in all imaging modes but rod visibility varied (Fig. S2); it should be noted that rod imaging was not optimized in confocal (and perhaps offset-aperture) as a relatively large aperture and long wavelength of light was used. Most cones had a characteristic appearance in

offset-aperture of an intensity gradient across the cell, with the gradient oriented orthogonal to offset direction. This asymmetry is illustrated in the SD image (Fig. 1X), where brighter pixels represent higher SD and most cones appear as bright rings. Differencing offset-aperture images enhanced photoreceptor contrast (Fig. 1Y). Low spatial frequency contrast that may be derived from the absorption/scattering properties of the underlying retinal pigment epithelium or choroid was visible at all offsets.

Offset-aperture images of humans similarly showed an oriented gradient of intensity across most cones (Fig. S3). Confocal AOSLO images of an AMD patient showed gaps in the cone mosaic (Fig. S3E, arrow), but multioffset images revealed cones in corresponding areas (e.g., Fig. S3N, arrow). Offset-aperture images could be combined in numerous ways to enhance contrast (Fig. S3 J–N). Feature contrast usually improved when offset-aperture images were differenced and could appear very similar to split-detection (Fig. S3O), depending on the images combined. The best subjective feature contrast was often generated when images from aperture positions on exact opposite sides of the point spread function (PSF) were differenced; however, this was not always the case.

It is often difficult to visualize cones in confocal AOSLO (Fig. 2A) in areas where drusen or early atrophy are seen clinically (Fig. S4); these cones may be misaligned, lacking outer segments, or lost completely. However, more cones could be visualized near drusen and in areas of early atrophy in multioffset images (Fig. 2B). A contiguous mosaic of cones was seen in some regions where cones were not visible in the confocal image (Fig. 2, arrows). Multioffset images also revealed discrete circular substructures within drusen (Fig. 2B, arrowhead); corresponding areas contained structures consistent with cones in the confocal image (Fig. 2A, arrowhead).

**Focusing Through the Retina.** Multioffset is compared with TPEF and confocal at multiple focal planes in a monkey in Fig. 3. As demonstrated previously (26), mosaic-like or lamina-like structures were visible in TPEF images captured at different planes throughout the retinal thickness (Fig. 3, Center column). These structures were indistinct at some focal planes (Fig. 3 E and H) but cells were visible at the RGC layer (Fig. 3B), where they appeared as bright TPEF surrounded by a dark center (presumably the cell nucleus) (26, 28, 29). Multioffset images showed similar cellular features (Fig. 3C) that were often in nearly perfect register with the cells seen in TPEF (Fig. S5). Corresponding confocal images (Fig. 3A) lacked the characteristic pattern of axon bundles typically seen, as these bundles are sparse or not present in this area of the temporal raphe.

Similar to TPEF, contrast for mosaic-like features was diminished in multioffset at the next two deeper focal planes (Fig. 3 F

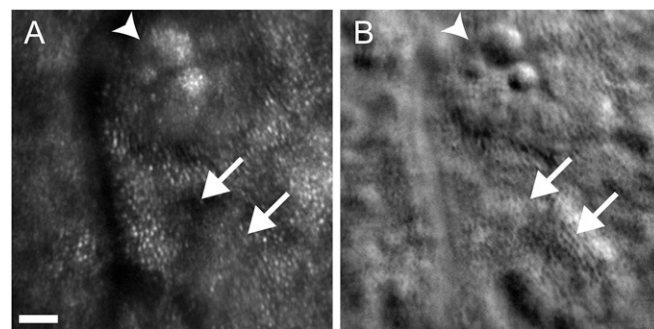


**Fig. 2.** Cones were not visible in some areas adjacent to drusen or on margin of hypo-autofluorescence (see Fig. S4) in confocal AOSLO (A, arrows) but multioffset images (B, arrows) showed a contiguous cone mosaic in some of these regions. Drusen substructures were seen in multioffset images as well circumscribed circular features (B, arrowhead); cones were visible at corresponding locations in confocal image (A, arrowhead). Corresponding clinical images are shown in Fig. S4. (Scale bar,  $50 \mu\text{m}$ .)

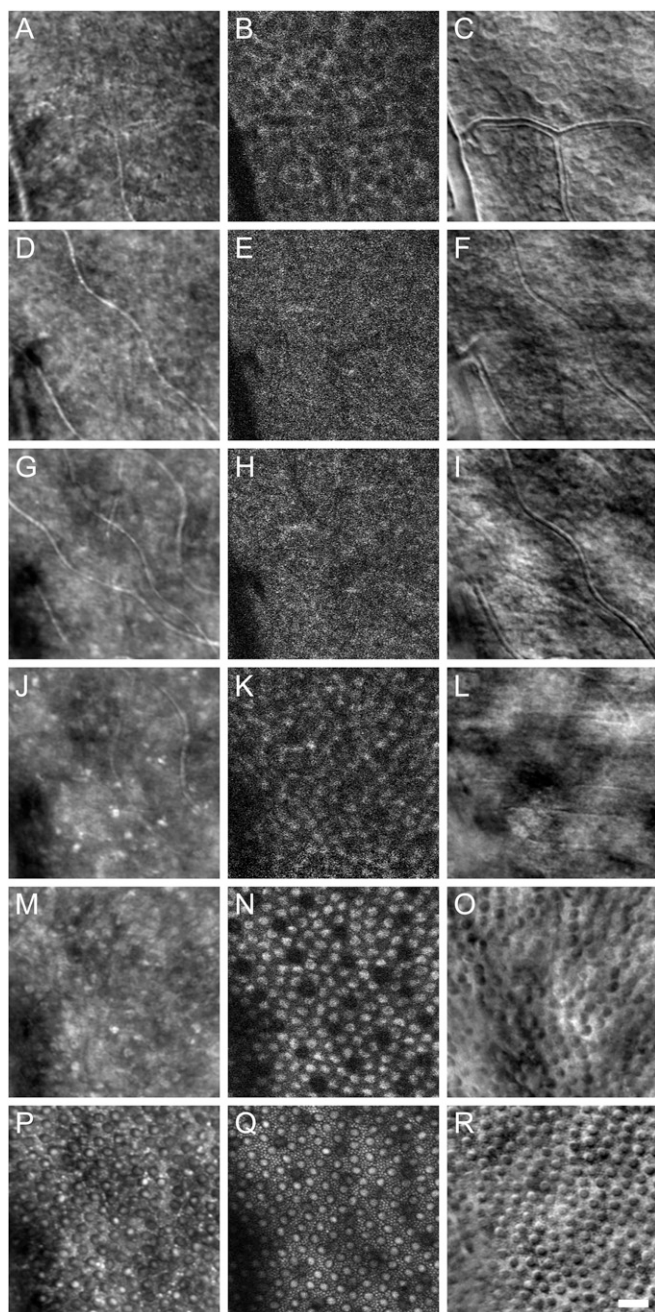


**Fig. 3.** Confocal (Left column: A, D, G, J, M, P), TPEF (Center column: B, E, H, K, N, Q), and multioffset (Right column: C, F, I, L, O, R) AOSLO images at several focal planes in a monkey. Cell somas were visible in the ganglion cell layer in TPEF (B) and multioffset (C) images but not confocal (A). Focal planes between the outer and inner layers contained laminar and mosaic-like structures in TPEF (E and H) and multioffset (F and I). Photoreceptor somas may be visible in TPEF and multioffset at the next focal plane (K and L). When focused at a more inner plane, cones appeared differently in multioffset (O) than at a deeper plane (R), where they appear similar to cones in split-detection. Approximate axial depth relative to the ganglion cell layer: (A–C) 0  $\mu\text{m}$ ; (D–F) 36  $\mu\text{m}$ ; (G–I) 69  $\mu\text{m}$ ; (J–L) 102  $\mu\text{m}$ ; (M–O) 140  $\mu\text{m}$ ; (P–R) 182  $\mu\text{m}$ . Retinal eccentricity is  $\sim 4$  mm from the fovea along the horizontal meridian within the temporal raphe. (Scale bar, 25  $\mu\text{m}$ .)

and I). Retinal blood vessels (and the cells flowing through them) are usually the only well-defined microscopic structures visible in confocal AOSLO between the inner and outer layers of the neural retina (12) and, as expected, vessels were visible in confocal images

at these planes (Fig. 3 D, G, and J) but little other discernable cellular structure was seen. When focused on the lumen of a blood vessel in these intermediate focal planes, certain multioffset detection configurations either enhanced or nearly completely minimized vessel contrast (Fig. S6).

TPEF and multioffset images from the same layers appeared to contain some different information, particularly at inner and intermediate layers. It is possible that photoreceptor nuclei were visible in multioffset at a focal plane just above the photoreceptor inner segments (Fig. 3L); this image also contained structures that appeared as horizontal striations, the origin of which is unknown. Putative cone inner segments were discernable in both TPEF and multioffset at the next deeper focal plane (Fig. 3N and O). As shown in Fig. 1, rods and cone outer segments were visible in all imaging modalities at the deepest focal plane imaged (Fig. 3P–R). Some sparsely arranged cones appeared darker in TPEF images (Fig. 3K, N, and Q); these were most likely S-cones that, because of their relative insensitivity to the two-photon excitation wavelength, produced less retinol (the candidate fluorophore) than L- and M-cones.

**Inner Retina.** RGC layer somal contrast varied depending on distance from the PSF (Fig. 4). Offset-aperture images from positions nearest to the PSF [offset = 8 Airy disk diameter (ADD)] did not contain visually discernable somas (Fig. 4A). It was only at the more distant aperture positions ( $\sim 13.7$ – $20.1$  ADD) that they became visible (Fig. 4B and C). The SD image from all offset-aperture images enhanced the contrast of some cells, particularly those near a large blood vessel (Fig. 4D, Left). Differencing of offset-aperture images from the more distant positions improved cell contrast substantially (Fig. 4E and F). However, not all cells were visible across the field-of-view of a single difference image (compare arrows and arrowheads in Fig. 4E and F). Averaging several multioffset images allowed somas to be visualized across the entire field-of-view (Fig. 4G). Distinct subcellular features were visible within some somas, including putative cell nuclei and nucleoli (Fig. 4H–K). High light levels were not required to obtain images of individual somas, as the same cells were visible at the lower levels typically used in humans (Fig. S7).

Cellular structure consistent with inner retinal neuron somas was also seen in multioffset images of the RGC layer of two different normal human eyes (Fig. 5). Somas were visible in each despite minor differences in detection pattern. Images in Fig. 5A were acquired with a radial sampling pattern (3.4 ADD aperture; 11.9 ADD offset;  $36^\circ$  intervals) using near infrared (NIR) light; the averages of three offset-aperture images were differenced to generate the multioffset image (similar to Fig. S3M). Images in Fig. 5B were also acquired using NIR light with a radial sampling pattern but with a larger aperture and greater offset (7.2 ADD aperture; 13.4 ADD offset;  $60^\circ$  intervals); several difference images were averaged to generate the multioffset image in Fig. 5B (similar to Fig. 4G). Overlying axon bundles did not appear to obstruct cell somas, as they were visible even in locations where axon bundles were present in the confocal image (Fig. S8B) and often lined up along the axon bundles. This characteristic morphology of RGC layer neurons known from *ex vivo* microscopy (30) was also seen in monkey images (Fig. S9).

Mean equivalent somal diameter was 12.8  $\mu\text{m}$  (range: 4–31.9; SD: 3.9;  $n = 502$ ) for the monkey images and 12.6  $\mu\text{m}$  (range: 5.2–22; SD: 2.7;  $n = 492$ ) for the human images. Mean somal area was 141.6  $\mu\text{m}^2$  (range: 12.9–797; SD: 87.5;  $n = 502$ ) for the monkey images and 130.7  $\mu\text{m}^2$  (range: 21.2–382.2; SD: 55.3;  $n = 492$ ) for the human images. The distribution of cell sizes computed for the  $\sim 500$  cells segmented from RGC layer images of each species (one monkey and two humans), from images shown herein (e.g., in Figs. 4 and 5 and Fig. S9), and additional images of surrounding areas, were within the range expected from the literature (Fig. 6 and Fig. S10).

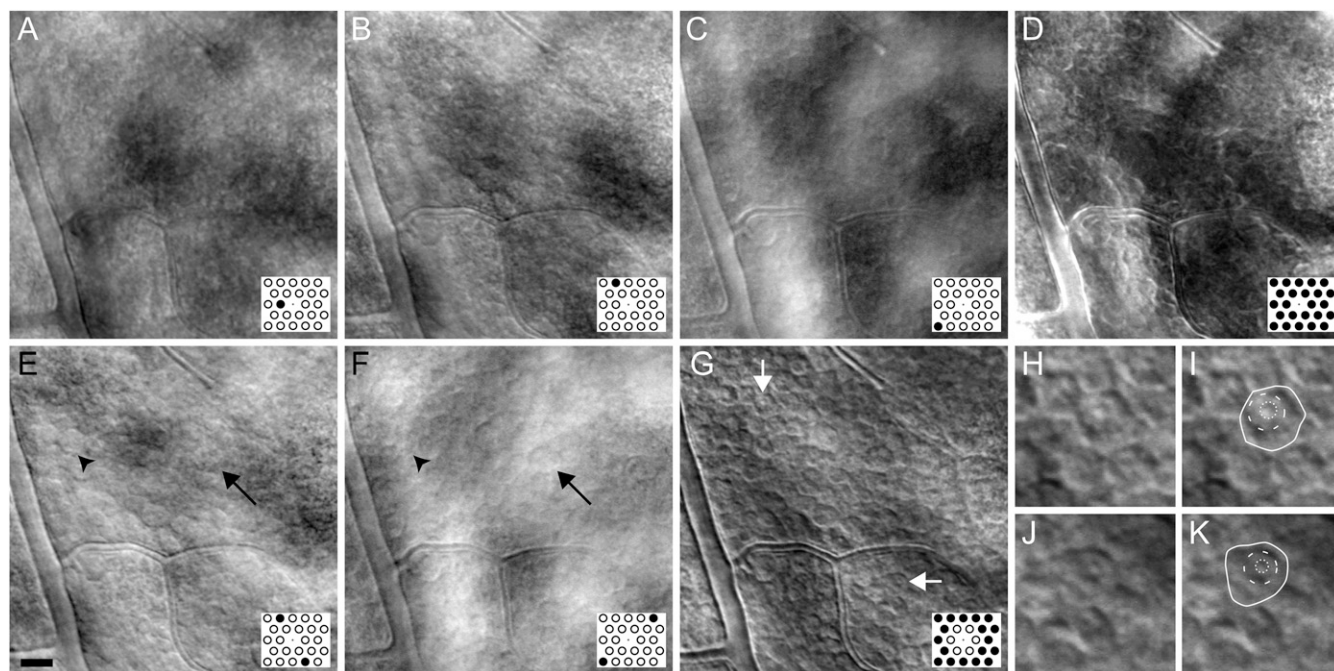


**Fig. 4.** Somas were not visible in offset-aperture images nearest to the PSF (A) but were visible at more distant positions (B and C). The SD image increased the contrast of some somas, particularly cells adjacent to a blood vessel on the left edge (D). Multi-offset difference images enhanced somal contrast (E and F), but not all cells were visible across each image (e.g., cell in E, arrowheads vs. cell in F, arrows). Averaging many difference images and enhancing local contrast with contrast limited histogram equalization, improved cell contrast, and visualized cells across the entire field-of-view (G). Some cells had visible subcellular structures (H–K). Arrows in G denote locations of H–K. Somas outlined with solid lines (I and K) contained putative nuclei (dashed circles) and nucleoli (dotted circles). Insets in A–G show detection pattern; shaded circle is aperture position of offset-aperture image (A–C) or multi-offset images (D–G); dot is 1 ADD and denotes PSF center; aperture diameter:  $\sim 4$  ADD; offsets centered from  $\sim 8$ –21 ADD. Image from raphe of macaque ( $\sim 4$  mm from fovea). (Scale bar in E, 25  $\mu\text{m}$  and applies to A–G; H–K are 50  $\mu\text{m} \times 50 \mu\text{m}$ .)

## Discussion

Individual somas of RGC layer neurons can be imaged directly in the living eye of monkeys and humans using existing AOSLO instrumentation with only minor modifications. Photoreceptor pathology in AMD can also be visualized with this method that enhances cone contrast in a similar manner to split-detection (24). The capability to image individual neurons through the full thickness of the retina could be transformative for the study of human retinal diseases. However, the demonstration of an imaging capability in a small number of eyes, such as we have shown here, does not necessarily guarantee that it can be quickly deployed productively in the clinic. As we have seen with the development of *in vivo* photoreceptor imaging (31), for example, improvements are still being made two decades later to translate this capability into a clinically useful tool. Human images of RGC layer neurons did not match the quality of those from the monkey for several reasons, chief among them being the much lower light levels used for safety concerns. Nonetheless, refinements using existing technologies, particularly those recently developed for autofluorescence imaging (32, 33), have the potential to improve image quality (*SI Materials and Methods*).

More work is needed to determine a success rate for multi-offset RGC layer imaging and document reproducibility in humans. Although the photoreceptor layer was successfully imaged in all eyes tested, we modified our detection strategy to improve RGC layer imaging as new data were acquired, so each individual was not imaged using the same detection configuration, preventing a success rate from being determined from the present data. Based on monkey results, it appears that many of our early attempts to image inner retinal neurons in humans were not successful because we did not use an appropriate combination of aperture size and offset. Monkey results demonstrated reproducibility (Fig. S7) and axial sectioning comparable to confocal AOSLO (Fig. 3), but the axial resolution of multi-offset

detection and its usefulness at eccentricities where the RGC layer is thicker and consists of many layers of cells needs further study.

Measurement of somal size in populations of RGC layer neurons may be advantageous for studying glaucoma pathogenesis and response to treatment, as mean RGC area has been shown to decrease in glaucoma before cell death (34). Subcellular resolution could also reveal *in vivo* the substantial changes that subcellular structures undergo during apoptosis in glaucoma (35). This level of resolution may also permit RGCs to be differentiated from the displaced amacrine cells that represent a larger proportion of RGC layer somas as distance from the fovea increases (36), although whether this is possible remains to be demonstrated. In humans, the percentage of amacrine cell somas in the RGC layer rises from  $\sim 15\%$  at 3 mm to  $\sim 25\%$  at 4 mm (36).

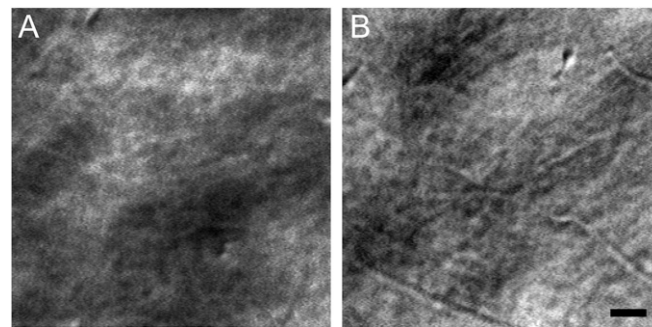


**Fig. 5.** Multi-offset images of ganglion cell layer neurons in the temporal retina ( $\sim 3.5$  mm from fovea) along the raphe (A) and superior to the raphe ( $\sim 3.5$  mm temporal,  $\sim 1.5$  mm superior of fovea) (B) from two different human eyes. (Scale bar, 50  $\mu\text{m}$ .)

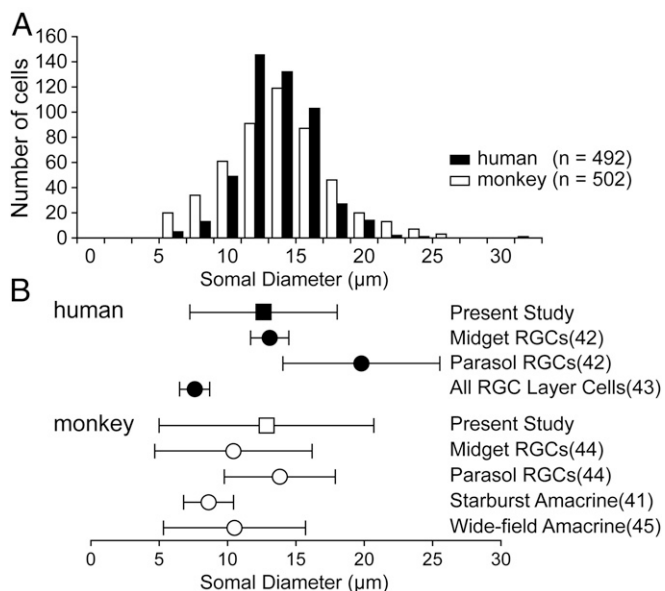


**Fig. 6.** Somal diameter distribution (A) was within the expected range (B). Means ( $\pm 2$  SD) are compared with values from the literature in B. Data points in B are mean ( $\pm 2$  SD) of measurements digitized for eccentricities of 2–4 mm from figures 4 in ref. 42, 8 in ref. 44, and 16 in ref. 41. Values are from text of ref. 43 for a 10-mm-diameter area centered on the fovea and from a retinal eccentricity of 4–8 mm for ref. 45.

Assuming monkey proportions are similar, ~20% of the cells in our images (from 3 to 4 mm) are likely displaced amacrine cells. Somas of several types of amacrine cells exist in the RGC layer. Some rare types have large somas similar in size to parasol RGCs (37), but most are relatively small (i.e., <10  $\mu\text{m}$  diameter) (36–38). We assume that the vast majority of cells in our sample are RGCs (75–85%), with ~95% of those being midget RGCs (39).

Somal size distributions (Fig. 6 and Fig. S10) fell within the expected range for the cell types assumed to be present based on data from the literature (34–45). However, this is the first in vivo dataset, so direct comparisons are not possible. Sharma et al. (26) did not measure somal diameter in their TPEF images; this would be difficult because TPEF contrast appears to be from the cell nucleus (26, 28, 29). We did not see a bimodal distribution of somal diameters, as Curcio et al. (36) did, likely because of the relatively smaller proportion of larger somas present in our samples from 3 to 4 mm than theirs at 5 mm, where the percentage of larger parasol RGCs is greater (~20%) (39). We saw only a small percentage of cells greater than 20  $\mu\text{m}$  in diameter (~3.5% in humans and ~8.8% in the monkey); these values are close to expectations from the literature for human, but perhaps a little high for monkey (36–44). However, it is likely that there are inaccuracies in our segmentation because of the low contrast of somas in the human images (Fig. S8 C and D) and because of the contrast of subcellular structures (such as putative cell nuclei) for some larger cells in monkey images (Fig. S5). More work is needed to develop unbiased segmentation methods for these images.

Despite the success of off-axis detection methods for visualizing retinal structure, they lack a complete theoretical framework. Elsner et al. (20, 23) have suggested light backscattered from the retina forms the core of the PSF that is detected in confocal imaging, whereas the light outside that area is more laterally scattered, multiply scattered, or scattered from different focal planes (20). In this framework, the scattering properties of the structures present at the position of the focused point source in the retina govern the proportion of light that falls within and outside the confocal detection area. For example, the strong waveguide properties of cones (46, 47) ensure that a large proportion of the light that returns from the photoreceptor layer is highly directionally backscattered, making

them particularly well-suited targets for confocal imaging; empirical results are consistent with this expectation.

Monkey photoreceptor layer results suggest that contrast enhancement for normal cones is not affected much by the direction or distance of the offset from the center of the PSF (Fig. 1). In the multiply scattered light-detection framework, it appears that light from healthy cones is symmetrically detectable in all directions outside the confocal area. Contrary to cones, blood vessels appear to be very asymmetrically scattering structures (Fig. S6), scattering light that interacts with them to areas outside the core of the PSF in a direction normal to the surface of the vessel wall. RGC layer somas were somewhat more variable, as some were visible regardless of offset direction (as long as the offset distance was sufficient) but not all cells could be seen across the field-of-view of each image (Fig. 4). It is not clear why a greater offset was required to image RGC layer neurons relative to photoreceptors and vasculature. We are currently developing an optical model to better understand this phenomenon and the mechanism of cellular contrast.

Some ambiguity exists as to the source of the signal in split-detection thought to arise from cone inner segments (24). Multi-offset images appeared similar to split-detection (24) at a focal plane assumed to be near the outer segments (Fig. 3R). However, at a plane assumed to be closer to the inner segments, their appearance changed (Fig. 3O). This may result from improved axial resolution in multioffset because of the smaller light-collection apertures used. Thus, some of the signal in split-detection attributed to inner segments may arise from the outer segments. It is possible that inner segments are visualized best in split-detection when outer segments are lost or misaligned. However, our results suggest that success in imaging misaligned cones in split-detection may depend on the orientation of the split. Future work is needed to more precisely compare these two closely related methods.

Multioffset detection may be advantageous for imaging some forms of pathology compared with split-detection where only a single detection configuration is possible (because of the fixed nature of the split). Similar to what Scoles et al. showed for achromatopsia with split-detection (24), the multioffset method could visualize cone structure in AMD patients in locations where cone presence was ambiguous or cones were absent in the confocal image. Our results suggest multioffset detection can be optimized to visualize cones altered by AMD (Fig. 2 and Fig. S3). Other features, such as the well-circumscribed discrete circular substructures within drusen that we observed (Fig. 2B, arrowhead), warrant further study and may provide insight into drusen formation and development. Future study should also be directed at more sophisticated sorting/combining of images and a more efficient mechanism for sampling the light distribution at the retinal conjugate focal plane.

A perhaps ideal approach would be to sample the entire focal plane with a matrix detector, where all “offsets” are acquired simultaneously. Such a detection scheme could be implemented in other imaging systems (e.g., scanning laser microscopy) and potentially be useful for imaging other nearly transparent tissues, such as neurons in the brain. Simultaneous acquisition could solve many problems encountered in human imaging; it would obviate the need for a separate confocal channel and ensure all images are acquired from the exact same location. Imaging duration could be substantially reduced, permitting the use of higher light levels that could further improve image quality. With sufficient detector sensitivity and sampling density, it would also allow for shaping of the detection configuration arbitrarily and after imaging (e.g., by binning detection units). This flexibility would allow images formed and combined to be altered in postprocessing to optimize them for the imaging conditions and structures of interest. We demonstrated here that when a point source is imaged onto the retina in AOSLO, valuable information exists across the entire aerial image plane; future work should determine the most efficient way to harvest this light.

## Materials and Methods

**Participants.** Participants consisted of 12 individuals with normal vision from the University of Rochester community and 5 AMD patients from the faculty practice

of one of the authors (M.M.C.). All participants gave written informed consent after the experiment was described both verbally and in writing. All experiments were approved by the research subjects review board of the University of Rochester and adhered to the tenets of the Declaration of Helsinki.

**Multioffset Imaging.** Experiments were carried out on three different AOSLO systems capable of simultaneous confocal and off-axis detection: a human research AOSLO (48, 49), a compact commercial prototype human AOSLO (50), and a nonhuman primate two-photon AOSLO (TPAOSLO) (26, 51). Some humans were imaged on both systems, permitting comparison between systems, but some major differences between them prevented direct comparisons (see *SI Materials and Methods* for details). On the research instruments, at each retinal location and focal plane, image sequences were obtained at several offset-aperture positions across the 2D retinal conjugate focal plane. Images were obtained at retinal eccentricities of 3–4 mm temporal to the fovea, within or superior to the raphe. Because of factors including light scatter, residual aberrations, and the double-pass nature of AOSLO, the PSF at the retinal conjugate focal plane is much broader than the theoretical ADD (22). However, for convenience and reproducibility, all detection parameters are expressed in these units. Aperture diameters tested ranged in size from ~1.2 to

9 ADD. Two detection patterns were used: “radial,” with apertures offset to a fixed distance from the center of the PSF at various angles (Fig. S1E), and “triangular,” with positions arranged in a triangular grid (Fig. S1F). We tested several different radial patterns in humans, in a range of offsets from 6 to 14 ADD, and both patterns in monkeys, with offsets extending to beyond 20 ADD. We imaged the outer retina in AMD patients and both inner and outer retina in normal eyes. Precision aperture positioning and image-processing methods are described in detail in *SI Materials and Methods*.

**Macaque Experiments.** For macaque experiments, animals were handled in accordance with the protocols prescribed and approved by the University of Rochester’s committee for animal research and in accordance with the Association for Research in Vision and Ophthalmology Animal Statement for the Use of Animals in Ophthalmic and Vision Research.

**ACKNOWLEDGMENTS.** This work was funded by NIH Grants EY021786, EY001319, EY014375, EY004367, EY022371, AG043645, EY007125, and EY025497; a grant from Canon, Inc.; a grant from the Edward N. & Della L. Thome Memorial Foundation (to M.M.C.); and a grant to the University of Rochester Department of Ophthalmology from Research to Prevent Blindness.

1. Polyak SL (1941) *The Retina* (Univ of Chicago Press, Chicago).
2. Bourne RRA, et al.; Vision Loss Expert Group of the Global Burden of Disease Study (2014) Prevalence and causes of vision loss in high-income countries and in Eastern and Central Europe: 1990–2010. *Br J Ophthalmol* 98(5):629–638.
3. Jackson GR, Owsley C, Curcio CA (2002) Photoreceptor degeneration and dysfunction in aging and age-related maculopathy. *Ageing Res Rev* 1(3):381–396.
4. Holz FG, Pauleikhoff D, Klein R, Bird AC (2004) Pathogenesis of lesions in late age-related macular disease. *Am J Ophthalmol* 137(3):504–510.
5. Quigley HA (2011) Glaucoma. *Lancet* 377(9774):1367–1377.
6. Balendra SI, Normando EM, Bloom PA, Cordeiro MF (2015) Advances in retinal ganglion cell imaging. *Eye (Lond)* 29(10):1260–1269.
7. Busse II, Wollstein G, Schuman JS (2014) OCT for glaucoma diagnosis, screening and detection of glaucoma progression. *Br J Ophthalmol* 98(Suppl 2):ii15–ii19.
8. Kardon RH (2011) Role of the macular optical coherence tomography scan in neuro-ophthalmology. *J Neuroophthalmol* 31(4):353–361.
9. Harwerth RS, Vilupuru AS, Rangaswamy NV, Smith EL, 3rd (2007) The relationship between nerve fiber layer and perimetry measurements. *Invest Ophthalmol Vis Sci* 48(2):763–773.
10. Liang J, Williams DR, Miller DT (1997) Supernormal vision and high-resolution retinal imaging through adaptive optics. *J Opt Soc Am A Opt Image Sci Vis* 14(11):2884–2892.
11. Rossi EA, et al. (2011) Imaging retinal mosaics in the living eye. *Eye (Lond)* 25(3):301–308.
12. Roorda A, et al. (2002) Adaptive optics scanning laser ophthalmoscopy. *Opt Express* 10(9):405–412.
13. Sincich LC, Zhang Y, Tiruveedhula P, Horton JC, Roorda A (2009) Resolving single cone inputs to visual receptive fields. *Nat Neurosci* 12(8):967–969.
14. Rossi EA, Roorda A (2010) The relationship between visual resolution and cone spacing in the human fovea. *Nat Neurosci* 13(2):156–157.
15. Carroll J, Neitz M, Hofer H, Neitz J, Williams DR (2004) Functional photoreceptor loss revealed with adaptive optics: An alternate cause of color blindness. *Proc Natl Acad Sci USA* 101(22):8461–8466.
16. Talcott KE, et al. (2011) Longitudinal study of cone photoreceptors during retinal degeneration and in response to ciliary neurotrophic factor treatment. *Invest Ophthalmol Vis Sci* 52(5):2219–2226.
17. Zhang Y, et al. (2014) Photoreceptor perturbation around subretinal drusenoid deposits as revealed by adaptive optics scanning laser ophthalmoscopy. *Am J Ophthalmol* 158(3):584–96.e1.
18. Song H, et al. (2015) Cone and rod loss in Stargardt disease revealed by adaptive optics scanning laser ophthalmoscopy. *JAMA Ophthalmol* 133(10):1198–1203.
19. Yoshida A, Ishiko S, Akiba J, Kitaya N, Nagaoka T (1998) Radiating retinal folds detected by scanning laser ophthalmoscopy using a diode laser in a dark-field mode in idiopathic macular holes. *Graefes Arch Clin Exp Ophthalmol* 236(6):445–450.
20. Elsner AE, Burns SA, Weiter JJ, Delori FC (1996) Infrared imaging of sub-retinal structures in the human ocular fundus. *Vision Res* 36(1):191–205.
21. Amos WB, Reichelt S, Cattermole DM, Laufer J (2003) Re-evaluation of differential phase contrast (DPC) in a scanning laser microscope using a split detector as an alternative to differential interference contrast (DIC) optics. *J Microsc* 210(Pt 2):166–175.
22. Scoles D, Sulai YN, Dubra A (2013) In vivo dark-field imaging of the retinal pigment epithelium cell mosaic. *Biomed Opt Express* 4(9):1710–1723.
23. Chui TYP, Vannasdale DA, Burns SA (2012) The use of forward scatter to improve retinal vascular imaging with an adaptive optics scanning laser ophthalmoscope. *Biomed Opt Express* 3(10):2537–2549.
24. Scoles D, et al. (2014) In vivo imaging of human cone photoreceptor inner segments. *Invest Ophthalmol Vis Sci* 55(7):4244–4251.
25. Hunter JJ, et al. (2010) Images of photoreceptors in living primate eyes using adaptive optics two-photon ophthalmoscopy. *Biomed Opt Express* 2(1):139–148.
26. Sharma R, Williams DR, Palczewska G, Palczewski K, Hunter JJ (2016) Two-photon autofluorescence imaging reveals cellular structures throughout the retina of the living primate eye. *Invest Ophthalmol Vis Sci* 57(2):632–646.
27. Elsner A, et al. (2000) Multiply scattered light tomography and confocal imaging: Detecting neovascularization in age-related macular degeneration. *Opt Express* 7(2):95–106.
28. Gualda EJ, Bueno JM, Artal P (2010) Wavefront optimized nonlinear microscopy of ex vivo human retinas. *J Biomed Opt* 15(2):026007.
29. Palczewska G, Golczak M, Williams DR, Hunter JJ, Palczewski K (2014) Endogenous fluorophores enable two-photon imaging of the primate eye. *Invest Ophthalmol Vis Sci* 55(7):4438–4447.
30. Snodderly DM, Weinhaus RS, Choi JC (1992) Neural-vascular relationships in central retina of macaque monkeys (*Macaca fascicularis*). *J Neurosci* 12(4):1169–1193.
31. Miller DT, Williams DR, Morris GM, Liang J (1996) Images of cone photoreceptors in the living human eye. *Vision Res* 36(8):1067–1079.
32. Zhang J, et al. (2015) An adaptive optics imaging system designed for clinical use. *Biomed Opt Express* 6(6):2120–2137.
33. Yang Q, et al. (2014) Closed-loop optical stabilization and digital image registration in adaptive optics scanning light ophthalmoscopy. *Biomed Opt Express* 5(9):3174–3191.
34. Weber AJ, Kaufman PL, Hubbard WC (1998) Morphology of single ganglion cells in the glaucomatous primate retina. *Invest Ophthalmol Vis Sci* 39(12):2304–2320.
35. Quigley HA, et al. (1995) Retinal ganglion cell death in experimental glaucoma and after axotomy occurs by apoptosis. *Invest Ophthalmol Vis Sci* 36(5):774–786.
36. Curcio CA, Allen KA (1990) Topography of ganglion cells in human retina. *J Comp Neurol* 300(1):5–25.
37. Sagar SM, Marshall PE (1988) Somatostatin-like immunoreactive material in associational ganglion cells of human retina. *Neuroscience* 27(2):507–516.
38. Hutchins JB, Hollyfield JG (1987) Cholinergic neurons in the human retina. *Exp Eye Res* 44(3):363–375.
39. Dacey DM (1993) The mosaic of mid-ganglion cells in the human retina. *J Neurosci* 13(12):5334–5355.
40. Mariansi AP, Hersh LB (1988) Synaptic organization of cholinergic amacrine cells in the rhesus monkey retina. *J Comp Neurol* 267(2):269–280.
41. Rodieck RW (1989) Starburst amacrine cells of the primate retina. *J Comp Neurol* 285(1):18–37.
42. Rodieck RW, Binmoeller KF, Dineen J (1985) Parasol and mid-ganglion cells of the human retina. *J Comp Neurol* 233(1):115–132.
43. Harman A, Abrahams B, Moore S, Hoskins R (2000) Neuronal density in the human retinal ganglion cell layer from 16–77 years. *Anat Rec* 260(2):124–131.
44. Watanabe M, Rodieck RW (1989) Parasol and mid-ganglion cells of the primate retina. *J Comp Neurol* 289(3):434–454.
45. Manookin MB, Puller C, Rieke F, Neitz J, Neitz M (2015) Distinctive receptive field and physiological properties of a wide-field amacrine cell in the macaque monkey retina. *J Neurophysiol* 114(3):1606–1616.
46. Enoch JM (1963) Optical properties of the retinal receptors. *J Opt Soc Am* 53(1):71–85.
47. Roorda A, Williams DR (2002) Optical fiber properties of individual human cones. *J Vis* 2(5):404–412.
48. Dubra A, Sulai Y (2011) Reflective afocal broadband adaptive optics scanning ophthalmoscope. *Biomed Opt Express* 2(6):1757–1768.
49. Rossi EA, et al. (2013) In vivo imaging of retinal pigment epithelium cells in age-related macular degeneration. *Biomed Opt Express* 4(11):2527–2539.
50. Saito K, et al. (2014) Rods and cones imaged with a commercial adaptive optics scanning light ophthalmoscope (AOSLO) prototype. *Invest Ophthalmol Vis Sci* 55(13):1594.
51. Sharma R, et al. (2016) In vivo two-photon fluorescence kinetics of primate rods and cones. *Invest Ophthalmol Vis Sci* 57(2):647–657.
52. Morgan JIW, Dubra A, Wolfe R, Merigan WH, Williams DR (2009) In vivo autofluorescence imaging of the human and macaque retinal pigment epithelium cell mosaic. *Invest Ophthalmol Vis Sci* 50(3):1350–1359.
53. Yang Q, et al. (2015) Calibration-free sinusoidal rectification and uniform retinal irradiance in scanning light ophthalmoscopy. *Opt Lett* 40(1):85–88.
54. Granger C, et al. (2016) Contiguous mapping of retinal pigment epithelium (RPE) cell morphometry across the horizontal meridian of the living human eye. *Invest Ophthalmol Vis Sci* 57(12).

# Supporting Information

Rossi et al. 10.1073/pnas.1613445114

## SI Materials and Methods

**Animal Preparation.** Three macaque monkeys, two *Macaca fascicularis* (5-y-old female and 9-y-old male) and one *Macaca mulatta* (12-y-old male), were imaged for these experiments. AOSLO images were obtained using contact lenses to correct for refractive error and carried out under general anesthesia with ketamine (5–20 mg/kg), midazolam (0.25 mg/kg), glycopyrrolate (0.017 mg/kg), and isoflurane (1.5–3%), and paralysis with rocuronium bromide (20–55  $\mu\text{g/kg/h}$ ). Pupil dilation and cycloplegia was induced with phenylephrine hydrochloride [2.5% (wt/vol)] and tropicamide (1%). Further details of the animal preparation are provided elsewhere (26).

**Imaging Systems.** For human experiments using the research instrument (48, 49), images were obtained with simultaneous visible [ $\lambda$  maximum: 680 nm; full width-half maximum (FWHM): 8 nm] and NIR ( $\lambda$  maximum: 796 nm; FWHM: 14 nm) superluminescent diode (SLD) illumination. The field-of-view was  $\sim 1.5^\circ$  square and images were acquired at 20 frames per second (fps) with  $\sim 80 \mu\text{W}$  of visible light and  $\sim 280 \mu\text{W}$  of NIR light. Confocal images were acquired from one channel and offset-aperture images were obtained from the other. Experiments were carried out with a visible confocal channel and NIR offset-aperture channel and vice versa. Detection channels were configured for automated positioning of the confocal aperture (described in detail below). Additional system details are provided elsewhere (48, 49).

The commercial AOSLO prototype (50) differed from the research instrument in some key aspects. Wavefront compensation was provided by two liquid crystal on silicon spatial light modulators instead of a deformable mirror, and avalanche photodiode (APD) detectors were used instead of photomultiplier tube (PMT) detectors. Illumination was provided with a longer wavelength NIR SLD ( $\lambda$  maximum: 835 nm; FWHM: 55 nm) and aberrations were measured and corrected over a smaller 6.7-mm-diameter pupil. The field-of-view was smaller ( $1.2^\circ$  square) and images were acquired at a higher frame rate (32 fps) with  $\sim 290 \mu\text{W}$  of light. The system was configured for simultaneous confocal and split-detection, after Scoles et al. (24): a 1 ADD pinhole mirror sent the central portion of the PSF to a first APD for confocal imaging, whereas the light outside this area (within an  $\sim 15$  ADD circular aperture) was split with a knife-edge prism and sent to two additional APDs.

For monkey imaging on the TPAOSLO (26, 51), the system was configured with three imaging channels, permitting simultaneous acquisition of confocal, offset-aperture, and TPEF images. Confocal images were obtained with NIR SLD illumination ( $\lambda$  maximum: 793 nm; FWHM: 17 nm). Two-photon fluorescence was excited using a pulsed laser with a tunable central wavelength set to 730 nm; pulse-width was  $< 55$  fs with a repetition rate of 80 MHz. Field-of-view was  $\sim 1.1^\circ \times 1.3^\circ$  and frame rate was 20 fps. For TPEF imaging, the light level at the pupil was  $\sim 7$  mW; some offset-aperture images were acquired with lower light levels of  $\sim 270 \mu\text{W}$  (for example, see Fig. S7 B and C). Emitted TPEF was collected in the wavelength range from 400 to 550 nm. TPEF images sequences were acquired for  $\sim 200$  s at each location and focal plane. The third imaging channel was configured to collect the 730-nm two-photon excitation light in various offset-aperture configurations; this ensured that offset-aperture and TPEF channels were precisely cofocused. The offset-aperture channel was configured for rapid automated repositioning.

Automated aperture positioning on the research AOSLO and TPAOSLO systems was performed with an apparatus described

elsewhere (49). An automatic positioning algorithm (49) placed the pinhole at the position of peak intensity of the light distribution at the retinal conjugate focal plane. This allowed precise 3D determination of the position of the PSF maximum intensity, either by using a model eye for alignment or when aligned using the actual eye under examination. The latter was preferred and used in most cases, particularly for monkeys. Precise determination of the center of the PSF provided a point of reference for all offset-aperture positions. Positioning precision was limited by the servo motor actuators (Z812B, Thorlabs) minimum resolution of 29 nm and bidirectional repeatability of  $< 1.5 \mu\text{m}$  (as quoted by the manufacturer).

Automatic positioning was controlled with custom software written in MATLAB (The MathWorks) using the APT software Active X controls (Thorlabs) that communicated through a network interface to the FPGA-based image acquisition software. Offset position was set manually for human experiments, where a small number of offsets were collected at each focal plane (six to eight offsets) and automatically for monkey experiments that tested a greater number of positions per focal plane (up to 24 offsets). Image sequences were acquired for  $\sim 5$  s in monkeys and  $\sim 10$ – $20$  s in humans. In most cases, an initial confocal image was taken with the aperture centered on the PSF. PMT gain was increased manually as distance from the PSF increased, and set at a fixed level for each set of images obtained at equal offsets. For automatic positioning, a continuous image sequence was obtained with equal frame numbers acquired at each offset. Aperture motion intervals were tracked by the software, so frames during motion could be discarded. For automated sequences, the software prompted for a gain increase at each new distance and waited for user input before recording the end of each aperture motion interval. To avoid saturating the detector when running at high gain, motion sequences were programmed to avoid movements back toward the PSF.

**Image Processing.** Offset-aperture and TPEF images were coregistered using the simultaneously acquired confocal image as a reference for eye motion (52). Coregistration was performed on research instrument images after sinusoidal rectification (53), at the strip level, with a strip height of 16–64 pixels, using custom software and an algorithm described previously (33). Split-detection images were coregistered and averaged after sinusoidal rectification using custom software developed by the manufacturer (Canon). Human images were registered from the forward and backward scans to increase signal-to-noise ratio; monkey images were from the forward scan only. Thus, human image sequences consisted of  $\sim 200$ – $400$  frames per offset and monkey sequences consisted of  $\sim 100$  frames per offset. Successfully registered strips were averaged. The number of strips registered and averaged per image sequence varied depending upon eye motion, with  $\sim 5\%$  and  $\sim 10$ – $15\%$  of strips discarded in monkeys and humans, respectively, because of either low cross correlations from poor image quality or non-existent data (i.e., strip was out of reference frame field-of-view).

Multiple offset-aperture images were combined digitally in a similar way to split-detection (24) using simple arithmetic operations. When referring to images acquired from just one offset position, we use established nomenclature and call them “offset-aperture” images. When referring to images generated by combining two or more offset-aperture images digitally, we refer to these as “multioffset” images. A single reference frame was used to register all offset-aperture images from a given location and focal plane, ensuring that within-frame distortions from eye motion were

identical for all images acquired at each offset; this permitted the generation of multioffset images without introducing artifacts from the eye motion encoded into the different reference frames.

After Scoles et al. (24), split-detection images were created by digital differencing normalized by the sum. Custom MATLAB scripts using elements of the Image Processing Toolbox were used to generate multioffset images. We experimented with several types of simple image combinations. One set of multioffset images was generated by differencing each unique pair of images obtained at each offset and normalizing by the sum [in the same way as split-detection (24)]. A second type was generated by first averaging two or more offset-aperture images and then differencing those with other images that consisted of an average of two or more different offset-aperture images. To increase the contrast across the image field-of-view, we experimented with combining offset-aperture and multioffset images in other ways, such as by taking the average, SD, variance, and so forth. The number of possible image combinations grows rapidly as the number of offsets increases and images are combined as unique image combinations are found in an  $n$  choose  $k$  manner (e.g., for 24 offsets, the maximum we tested, there are 263 unique image pairs).

Images were sorted manually and those with the best subjective contrast selected for analysis. Large variations in low spatial frequency contrast often reduced the local contrast of small features; this was partially overcome by applying contrast-limited adaptive histogram equalization to multioffset images with the *adapthisteq* function in MATLAB, although care needed to be used when tuning function parameters as noise could be increased. As a final step to make images suitable for presentation, brightness and contrast were adjusted using MATLAB or Adobe Photoshop (Adobe Systems). Figures herein were assembled using Adobe Illustrator (Adobe Systems). Cell somas were segmented by manually tracing cell contours with a mouse or digital stylus and tablet PC (Surface Pro-3, Microsoft) in Photoshop. Binary images of cell contours were loaded into MATLAB and cell statistics were calculated using the *regionprops* function. The size of retinal features was calculated using methods described previously (26, 49).

## SI Discussion

Several aspects can be optimized to improve human imaging. First, more images at a greater number of offset positions (including more distant aperture positions than tested herein) could be used to yield a richer dataset, as was done for the monkey. For

light safety purposes, fewer offset-aperture images were collected in humans, only 6–8, usually at a fixed offset, whereas 24 were obtained in monkeys, at a variety of offsets. This shortened light-exposure duration but greatly limited the number and variety of image combinations and the increased signal-to-noise ratio possible with more images. Imaging duration (and/or light levels) could be increased and more offsets tested if solely NIR light was used instead of simultaneous NIR and visible illumination. This could easily be implemented optically by splitting off the confocal light using an annular mirror before multioffset detection [in a similar way to split-detection (24)] and then using that as the motion-reference channel. This single wavelength approach could also minimize any additional blur that may be introduced by the pupil motion that can cause the transverse chromatic aberration between imaging and motion reference wavelengths to change (54).

Retinal motion reduced the quality of human images compared with those from the anesthetized monkey that had only minimal motion induced by respiration. Even with careful fixation, the small imaging-field size and sequential imaging approach caused registered images from each offset to have a slightly different field-of-view. This approach substantially limited the region of overlap between all offset-aperture images available for multioffset image combinations. Another related problem was that eye motion necessitated the use of a larger field-of-view in the human than in the monkey (to facilitate image registration). This resulted in a lower pixel sampling density ( $\sim 0.9$   $\mu\text{m}$  per pixel in human vs.  $\sim 0.5$   $\mu\text{m}$  per pixel in monkey) that reduced the digitization fidelity of smaller features. These issues can be overcome with active eye tracking and optical image stabilization (32, 33).

Appropriate focus for RGC layer neuron imaging was challenging for both monkey and human experiments. The best images of RGC layer somas were only obtained at a single focal plane and images were very sensitive to focus position (this is partially illustrated in Fig. 3). TPEF imaging facilitated focusing in the monkey, where the best RGC layer focus could be found using outer retina TPEF; in the human, focusing was guided by nerve fiber bundle focus in confocal images of adjacent retinal locations where bundles were present (as we mostly imaged along the raphe) and by assuming the ganglion cell layer was just beneath the RNFL. A single-wavelength approach would be advantageous here as well because the difference in focus between the confocal and offset-aperture channels (because of longitudinal chromatic aberration) complicated focusing.



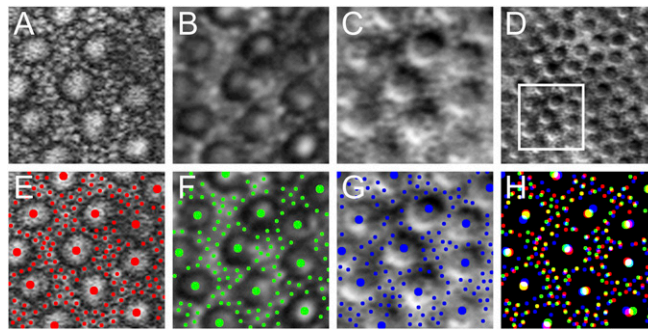


**Fig. S2.** Zoomed-in views of TPEF (*A*), confocal (*B*), and multioffset (*C*) images from Fig. 1 are shown here to illustrate that every cone was visible in all imaging modalities but rod visibility varied. Field-of-view of *A–C* and *E–H* is  $40 \times 40 \mu\text{m}$ ; square in *D* denotes location of zoomed-in views. Manually marked cone and rod locations are shown in *E–G* and are overlaid in *H* to show positional variability. In *H*, yellow denotes overlap of TPEF and confocal; magenta denotes overlap of TPEF and multioffset; cyan denotes overlap of confocal and multioffset and white denotes overlap of all three.

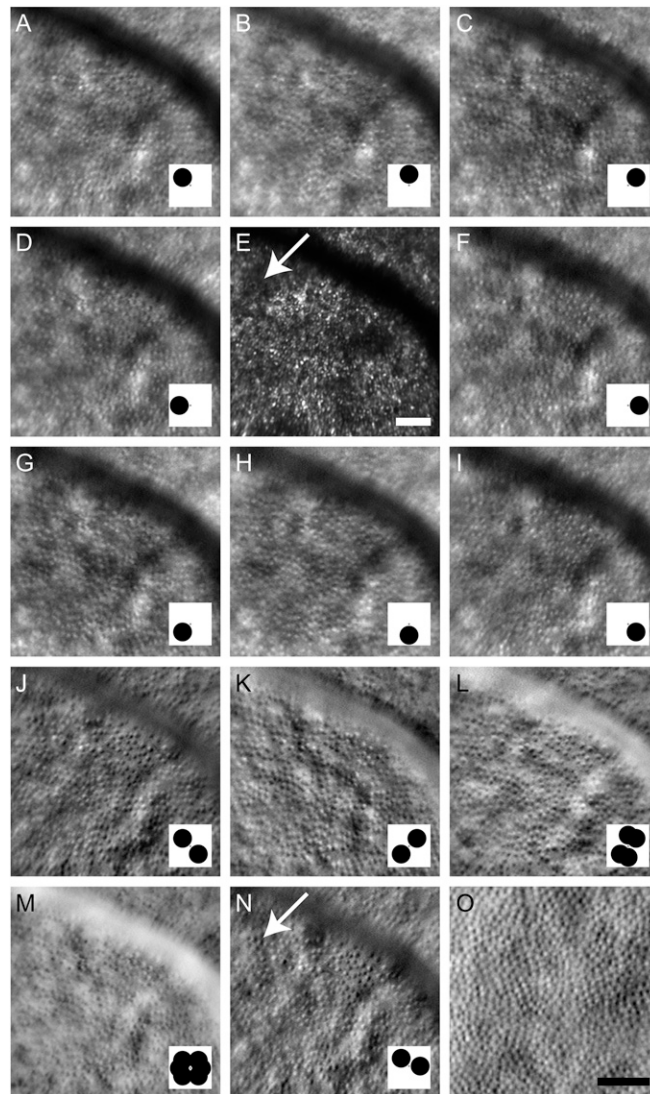


**Fig. S3.** Offset-aperture images (*A–D* and *F–I*) can be combined in numerous ways into multioffset images (*J–N*) that can appear similar to split-detection images (*O*) and reveal cones in AMD (*N*, arrow) that were not visible in confocal images (*E*, arrow). Offset-aperture images obtained with visible light (680 nm) using a radial sampling pattern (~9 ADD aperture; ~6 ADD offset; 45° intervals) in an area of the retina that appears normal on clinical examination in a patient with AMD (*A–D* and *F–I*); *Inset* denotes aperture position with respect to center of PSF (denoted with 1 ADD gray dot). Confocal image from NIR channel is shown in *E*. Multioffset images (*J–N*) can be generated in many ways, including: (i) difference of two aperture positions (*J*, *K*, *N*); (ii) difference of averages of two aperture positions (*L*) and difference of average of *B* and *C* and *G* and *H*; and (iii) difference of averages of three positions (*M*) and difference of average of *A*, *D*, *G* and *C*, *F*, *I*. Aperture positions differenced denoted in *Insets* of *J–N*. The multioffset image with the best subjective contrast was often but not always (*N*) obtained from aperture positions on exact opposite sides of the PSF. (Scale bars, 50 μm; scale bar in *E* applies to *A–N*.)

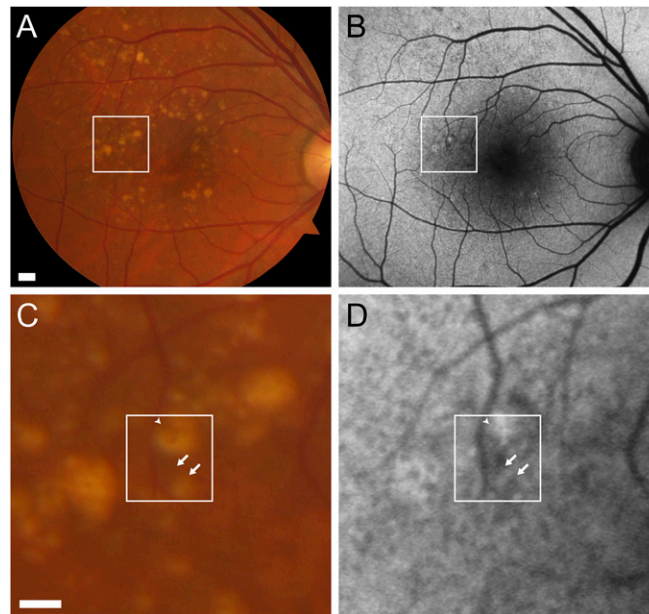


**Fig. 54.** Color fundus photography (*A* and *C*) and autofluorescence SLO (*B* and *D*) reveal gross drusen structure and patches of hypo-autofluorescence, suggestive of early atrophy in AMD. Squares in *A* and *B* reflect field-of-view of images below; squares in *C* and *D* reflect field-of-view of AOSLO images shown in Fig. 2; arrows and arrowheads are at their corresponding locations from Fig. 2. (Scale bars, 500  $\mu\text{m}$  in *A* and 200  $\mu\text{m}$  in *C*.)

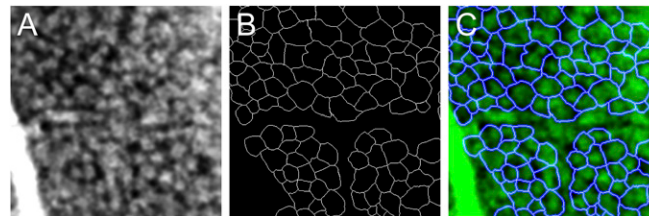


**Fig. 55.** The TPEF image shown in Fig. 3*B* is shown here inverted and smoothed with a three-pixel-wide Gaussian blurring filter here in *A*. The segmentation image from the multioffset image from Fig. 3*C* is shown here in *B*. These images are merged in *C* to show that the dark regions of the TPEF image (shown as green regions in *C*) often reside within the somas visible in the multioffset images. Images are 175  $\times$  175  $\mu\text{m}$ .

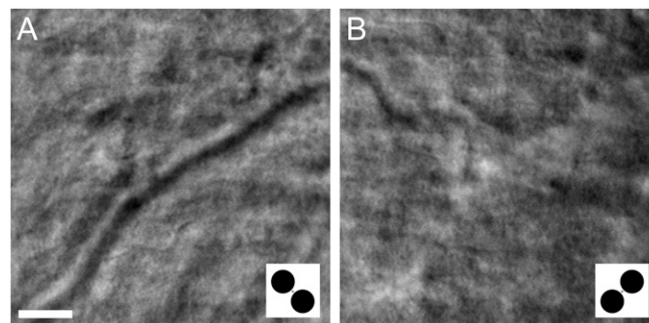


**Fig. 56.** Blood vessel contrast can be enhanced or nearly completely minimized depending on multioffset configuration. The contrast of the blood vessel running diagonally in *A* from lower left to upper right is enhanced with this multioffset configuration (*A*, *Inset*) but minimized in *B* with the orthogonal configuration (*B*, *Inset*). Images obtained from a normal human retina. (Scale bar, 50  $\mu\text{m}$ .)

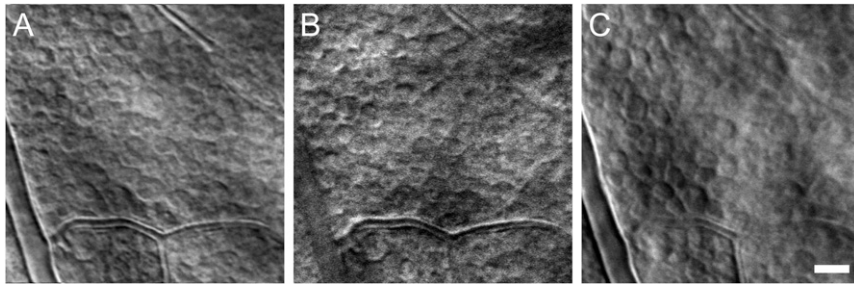


**Fig. 57.** Multi-offset images of ganglion cell layer neurons in monkeys with high light levels ( $\sim 7$  mW) required for TPEF (A) are still visible at the lower light levels ( $\sim 270$   $\mu$ W) typically used for human imaging with the same size aperture (B) or with an aperture with twice the diameter (C). (Scale bar, 25  $\mu$ m.)

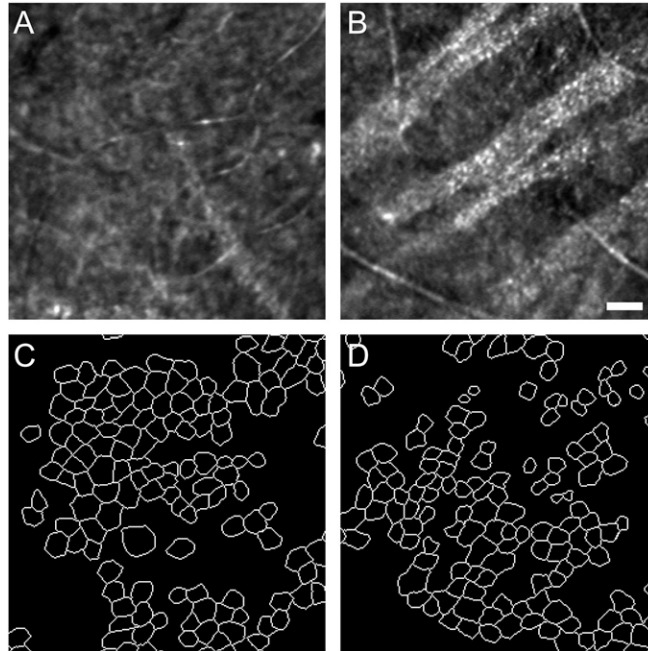


**Fig. 58.** Corresponding confocal images (A and B) from the locations of the multi-offset images shown in Fig. 5 show no discernible cell somas. Corresponding segmentation images (C and D) show the locations of the cell somas identified from the images shown in Fig. 5. (Scale bar, 50  $\mu$ m.)



**Fig. 59.** Confocal (A), multi-offset (B), and segmentation images (C) from an area superior to the raphe in a monkey shows characteristic pattern of ganglion cell layer somas lining up along the axon bundles of the nerve fiber layer. Multi-offset image is a difference of two offset-aperture images. (Scale bar, 50  $\mu$ m.)

